Editors' Suggestion   Featured in Physics

Dispersion-Selective Band Engineering in an Artificial Kagome Superlattice

Shuai Wang,[1,2,*] Zhen Zhan[ORCID],[3,4,*] Xiaodong Fan[ORCID],[1,2,*,†] Yonggang Li,[3] Pierre A. Pantaleón[ORCID],[4] Chaochao Ye,[1,2]
Zhiping He[ORCID],[1] Laiming Wei,[5] Lin Li,[1,2,6] Francisco Guinea,[4,7,‡] Shengjun Yuan[ORCID],[3,8,§] and Changgan Zeng[ORCID][1,2,6,‖]

[1]*CAS Key Laboratory of Strongly-Coupled Quantum Matter Physics, and Department of Physics,*
University of Science and Technology of China, Hefei, Anhui 230026, China
[2]*International Center for Quantum Design of Functional Materials (ICQD),*
Hefei National Research Center for Physical Sciences at the Microscale, University of Science and Technology of China,
Hefei, Anhui 230026, China
[3]*Key Laboratory of Artificial Micro- and Nano-structures of the Ministry of Education and School of Physics and Technology,*
Wuhan University, Wuhan, Hubei 430072, China
[4]*Imdea Nanoscience, Madrid 28015, Spain*
[5]*School of Advanced Manufacturing Engineering, Hefei University, Hefei, Anhui 230601, China*
[6]*Hefei National Laboratory, University of Science and Technology of China, Hefei, Anhui 230088, China*
[7]*Donostia International Physics Center, Paseo Manuel de Lardizabal 4, San Sebastian 20018, Spain*
[8]*Wuhan Institute of Quantum Technology, Wuhan, Hubei 430206, China*

The relentless pursuit of band structure engineering continues to be a fundamental aspect in solid-state research. Here, we meticulously construct an artificial kagome potential to generate and control multiple Dirac bands of graphene. This unique high-order potential harbors natural multiperiodic components, enabling the reconstruction of band structures through different potential contributions. As a result, the band components, each characterized by distinct dispersions, shift in energy at different velocities in response to the variation of artificial potential. Thereby, we observe a significant spectral weight redistribution of the multiple Dirac peaks. Furthermore, the magnetic field can effectively weaken the superlattice effect and reactivate the intrinsic Dirac band. Overall, we achieve actively dispersion-selective band engineering, a functionality that would substantially increase the freedom in band design.

Since the inception of band theory, researchers have been striving to manipulate band structures to achieve desired physical properties [1]. However, conventional band engineering methods, such as heterostructures [2], interfacial strain [3], and alloying [4], usually lack the capability for *in situ* and continuous control of the engineered band structures. The emergence of van der Waals (vdW) materials, especially graphene, offers opportunities for direct Fermi level tuning via gating [5] and even band structure engineering through moiré heterostructures [6]. This moiré-type periodic potential can effectively modify energy bands, leading to abundant emergent physics, such as correlated insulating states, unconventional superconductivity, ferromagnetism, ferroelectric, and (fractional) quantum anomalous Hall effect [7–16].

Alternatively, artificial superlattices, created by directly imposing designed periodic potentials, also provides remarkable capabilities for modulating the energy bands of two-dimensional electronic systems [17–21]. In contrast to moiré-type potentials, artificial lattices possess flexible control of the lattice patterns, lattice symmetry, and potential strength, extending new degrees of freedom for the on-demand design of band structures. Previous studies on artificial lattices, predominantly employing triangular or square lattices with periods less than 40 nm, yield replica Dirac cones, Landau fans, and Hofstadter spectrums [18,19,21], well reproducing the behaviors in graphene/ *h*-BN moiré systems [22].

In this study, we specifically design a kagome-type artificial superlattice with a large period of 80 nm, which enables the folding and compression of a variety of high-energy bands into the experimentally accessible low-energy regime. It is particularly noteworthy that the kagome superlattice introduces a unique high-order potential. Unlike triangle or square potentials, for the precise depiction of the kagome potential within the superlattice potential $V_{SL}(r)$ model (Note 1 in Supplemental Material [23]), at least a third-order Hamiltonian expansion is required:

$$\begin{aligned} V_{SL}(\boldsymbol{r}) &= U_0 + U_1 + U_2 + U_3 \\ &= U_0 + 6\alpha v_1 \cos(\boldsymbol{G}_1 \cdot \boldsymbol{r}) + 6\alpha v_2 \cos[(2\boldsymbol{G}_1 + \boldsymbol{G}_2) \cdot \boldsymbol{r}] \\ &\quad + 6\alpha v_3 \cos(2\boldsymbol{G}_2 \cdot \boldsymbol{r}), \end{aligned} \tag{1}$$

---

[*]These authors contributed equally to this letter.
[†]Contact author: fanxd@ustc.edu.cn
[‡]Contact author: paco.guinea@imdea.org
[§]Contact author: s.yuan@whu.edu.cn
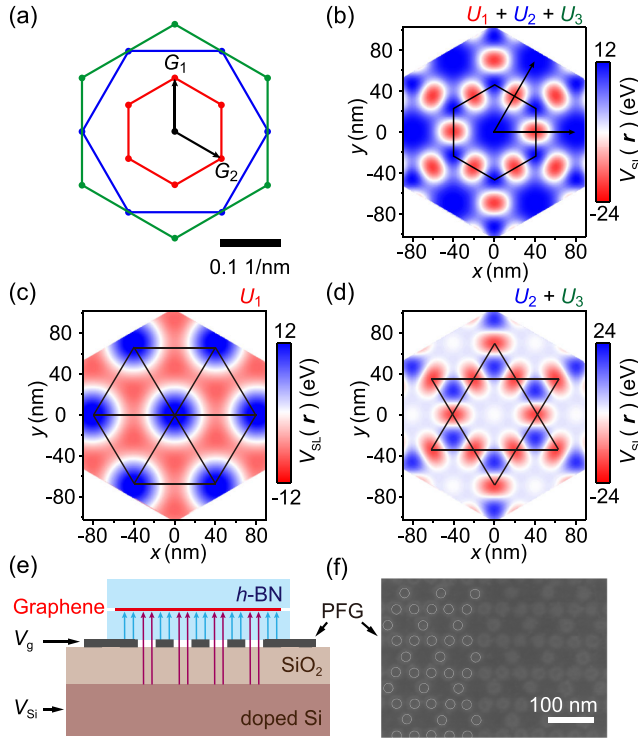[‖]Contact author: cgzeng@ustc.edu.cn

FIG. 1. High-order kagome potential and sample layout of the artificial kagome device. (a) Three harmonic components of a kagome superlattice potential. Points at the corner of each hexagon are the corresponding first (red), second (blue), and third (green) harmonics in the reciprocal space that defines U_1, U_2, and U_3 terms in Eq. (1). (b)–(d) Real-space distributions of the modeled potential with $U_1 + U_2 + U_3$ (b), U_1 (c), and $U_2 + U_3$ (d) terms, respectively. Black hexagon and black arrows in (b) are the primitive unit cell and the lattice vectors, respectively. The long-wavelength triangular component and shared-corner triangular component of the kagome potential are illustrated by black lines in (c) and (d), respectively. (e) Side-view schematic of the artificial-lattice device. V_g is applied on the prepatterned few-layer graphite (PFG). (f) Scanning electron microscopy image of the PFG with an artificial kagome-lattice pattern.

where the uniform component U_0 is set to be 0, α is a strength parameter, v_1, v_2, and v_3 are the harmonic coefficients, and G_1 and G_2 are the reciprocal lattice vectors of the kagome superlattice. As shown in Figs. 1(a)–1(d), this high-order potential harbors intrinsic multiperiodic components, allowing for the reconstruction of the band structure through different potential contributions. Specifically, this manifests as distinct contributing weights of various potential components to different types of band components. The flatband components mainly arising from $U_2 + U_3$ are more sensitive to be shifted by the variation of artificial potential compared to the linear-dispersion band components that originate from all Hamiltonian terms, thus resulting in dispersion-selective band modulation. This functionality would substantially increase the freedom in band design, paving the way to on-demand band design in the future.

Experimentally, we employed the standard vdW assembly technique [24] to fabricate the artificial-lattice device [19] as shown in Fig. 1(e) (Supplemental Note 2 [23]). Through standard electron beam lithography and reactive ion etching, a few-layer graphite was pre-patterned into a kagome-lattice shape [Fig. 1(f)] that functions as a local gate (V_g) for the graphene. On the other hand, the voltage supplied to the doped Si (V_{Si}) allows for further control over the chemical potential of partial graphene via the hollow region of the patterned graphite. It can be roughly considered that V_g and V_{Si} mainly control U_1 and $U_2 + U_3$ in Figs. 1(c) and 1(d), respectively. By independently adjusting V_g and V_{Si}, both the strength of artificial potential and the carrier density (n) of graphene can be finely tuned. Among them, n can be estimated using the capacitor model where the effective areas of different gates are considered (Supplemental Note 2 [23]) and the artificial potential strength is predominantly governed by V_{Si} [19] (Supplemental Note 3 [23]). Using a finite-element electrostatic simulation, we obtained the potential field distribution of this device configuration as illustrated in Supplemental Fig. S5 [23], which well reproduces the high-order potential in Fig. 1(b).

To probe the tuning effects of the artificial potential, we measured the n dependence of the longitudinal resistance (R_{xx}) at various V_{Si}. As shown in Figs. 2(a) and 2(b), the color plots of R_{xx} demonstrate a multistage change as the potential strength intensifies. At $V_{Si} = 20$ V, a distinct single Dirac peak corresponding to the intrinsic Dirac point (IDP) of graphene is observed. The carrier mobility exceeds
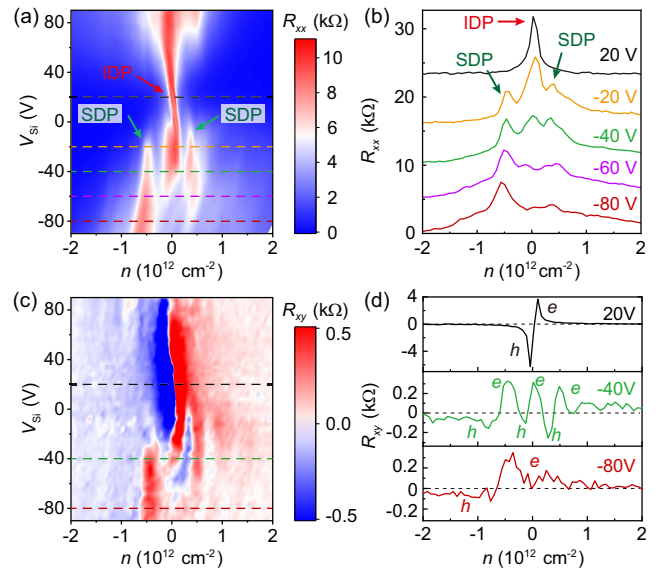

FIG. 2. Spectral weight redistribution of the multiple Dirac resistance peaks. (a),(b) Longitudinal resistance R_{xx} map as a function of n and V_{Si}, and corresponding line cuts, measured at $T = 1.5$ K. The curves in (b) are shifted for clarity. The red and green arrows point to the IDP and the SDPs, respectively. (c),(d) Hall resistance R_{xy} at $B = 0.1$ T as a function of n and V_{Si}, and corresponding line cuts.
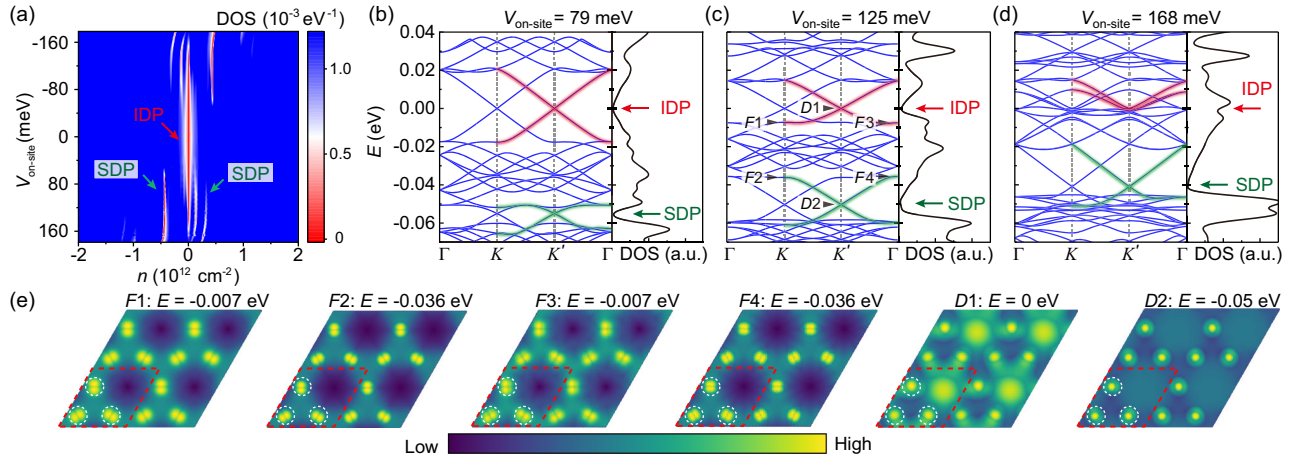
FIG. 3. Calculated DOS and band structures of the artificial kagome lattice. (a) DOS map as a function of n and $V_{\text{on-site}}$. (b)–(d) Band structures and DOS at different $V_{\text{on-site}}$, with the intrinsic Dirac bands and satellite Dirac bands highlighted by red and green, respectively. The red and green arrows in (a)–(d) point to the IDPs and SDPs, respectively. The zero-energy points are fixed at the IDPs for a better comparison with experiments (see Supplemental Fig. S10 [23]). (e) Distributions of electronic states in real space corresponding to the different sites marked in (c). The unit cell of the kagome superlattice and the artificial-lattice sites are outlined by the red dashed rhomboid and white dashed circles, respectively.

50 000 cm^2/V s when the carrier density is less than 2×10^{12} cm^{-2}, which confirms the quality of our device (Supplemental Note 2 [23]). When V_{Si} is set to -20 V, two satellite Dirac points (SDPs) emerge on either side of the IDP. This phenomenon resembles that seen in graphene modulated by artificial triangular or square lattices [18,19]. However, as V_{Si} further increases, the IDP begins to decay (green curve). When V_{Si} exceeds -60 V, the IDP becomes barely discernible, and the left SDP dominates the resistive extremum (purple and red curves).

This behavior is also corroborated by the corresponding Hall resistance (R_{xy}) at 0.1 T as shown in Figs. 2(c) and 2(d). As the superlattice potential rises, the charge neutral points (CNPs), separated by opposite Hall signals, undergo two obvious evolutions: Initially, they transition from a single carrier-type reversal (black curve) to multiple transitions induced by the superlattice minibands (green curve) and subsequently evolve to only one recognizable CNP determined by the left SDP (red curve). Therefore, a significant spectral weight redistribution of the multiple Dirac bands is achieved by increasing the kagome-lattice potential. This observation is consistently replicated across several samples (Supplemental Fig. S3 [23]).

To interpret the experimental results, we calculated the density of states (DOS) and band structures under different superlattice potentials based on the tight-binding model. To deal with the large-size unit cell of the superlattice (around 211 598 atoms), a rescaling method [30] and a tight-binding propagation approach [31] were implemented (Supplemental Note 4 [23]). The potential strength is represented by the on-site energy ($V_{\text{on-site}}$), which is defined as the extremum value of the hollow region in the super-lattice potentials. Figure 3(a) illustrates the DOS as a function of n and $V_{\text{on-site}}$, where the DOS minimum typically aligns with the resistance maximum in transport measurements. Remarkably, there is excellent agreement between the theoretical DOS [Fig. 3(a)] and the experimental R_{xx} [Fig. 2(a)]. The kagome-lattice potentials lead to the emergence of the DOS minimums that correspond to the newly formed SDPs (green arrows), which become increasingly prominent as $V_{\text{on-site}}$ escalates. On the other hand, the DOS minimum corresponds to the IDP (red arrow) is suppressed under strong potential, replicating the spectral weight redistribution of the multiple Dirac resistance peaks in Fig. 2.

Figures 3(b)–3(d) present the band structures and corresponding DOS spectrums in response to different $V_{\text{on-site}}$. More details are demonstrated in Supplemental Figs. S10 and S11 [23]. Because the intensity and evolution pattern of the SDP on the hole side are more pronounced in the experiment, we primarily focus on the hole-side SDP in the subsequent analysis. For $V_{\text{on-site}} = 79$ meV, the SDP indicated by the green arrow begins to appear. As $V_{\text{on-site}}$ increases to 125 meV, we observe a dramatic increase in the Fermi velocity of the SDP, while that of the IDP (red arrow) decreases to a level comparable with the SDP. When $V_{\text{on-site}}$ reaches 168 meV, the intrinsic Dirac band is further compressed and even submerged within other superlattice bands. Consequently, the DOS associated with the IDP no longer exhibits a clear minimum in the DOS spectrum.

This phenomenon can be ascribed to dispersion-selective band modulation by the high-order kagome potential. As illustrated in Fig. 1 and Supplemental Fig. S1 [23], in the Hamiltonian analysis of the superlattice potential (Supplemental Note 1 [23]), we need at least three harmonic components to accurately describe the artificial kagome

potential. This unique high-order potential possesses potential oscillations with distinct wavelengths λ [35], leading to band reconstructions of different energies as $E_r \sim 1/\lambda$. The long-wavelength triangular component [Fig. 1(c)] originates from the quantum confinement of the large hexagons of the patterned gate and is mainly defined by the first harmonic of the superlattice potential Hamiltonian. This potential, possessing a threefold rotational symmetry, primarily contributes to the replicas of intrinsic Dirac cones near 0.02 eV between Γ and K points [18,19,22], as shown in Fig. 3(b). Another superlattice component in the shared-corner triangular form [Fig. 1(d)] is generated by the quantum confinement at the kagome-lattice sites and primarily defined by the combined contributions of the second and third harmonics of the superlattice potential Hamiltonian. This potential mainly influences the shape of higher-energy bands.

On the other hand, the large period of the superlattice (80 nm) is also crucial for the dispersion-selective band engineering. Unlike the 10-nm-periodic artificial lattice (Supplemental Note 5 and Fig. S12 [23]), this larger superlattice period enables the folding and compression of a variety of high-energy bands into the experimentally accessible low-energy regime, including some nearly dispersionless bands [Fig. 3(c)]. These diverse band configurations provide a foundation for subsequent dispersion-selective band modulation. We primarily focus on the bands closely related to the IDP and SDP, which are marked by red and green in Fig. 3(c), respectively. We note that these bands are mainly composed of two typical components: One includes the bands with linear dispersions ($D1$ and $D2$) at the Dirac points, and the other comprises the nearly dispersionless bands ($F1$ and $F2$ at the K point and $F3$ and $F4$ at the Γ point).

We further calculated the real-space distributions of the electronic states for these different band components, as shown in Fig. 3(e). It is evident that the different band components present markedly distinct state distributions. For the dispersionless band components ($F1$–$F4$), the real-space states mainly localize at the kagome-lattice sites (white dashed circles), a typical feature of localized wave functions of dispersionless bands. This implies that the dispersionless band components originate from quantum confinement at the kagome-lattice sites. In other words, they mainly arise from the contributions of the second and third harmonic terms of the superlattice potential Hamiltonian [see Eq. (1) and Fig. 1(d)].

In contrast, for the band components with linear dispersion ($D1$ and $D2$), the real-space electronic states are delocalized and distribute not only at the kagome sites, but also over the long-wavelength triangular confined regions. The states of $D1$ are comparably distributed over different confined regions, while those of $D2$ show a peak at the kagome sites, accompanied by a secondary distribution in the triangular confined regions. These observations suggest that the linear band components ($D1$ and $D2$) arise from the combined effect of the quantum

confinements from both the triangular regions and kagome sites, which correspond to the combined contributions of all terms in the superlattice potential Hamiltonian [see Eq. (1) and Fig. 1]. The redistribution of the states for different Dirac cones results from the interplay between the quantum confinements of different wavelength regions.

Given that the artificial kagome potential is essentially a relative potential applied between the kagome sites and the spacing of them (Supplemental Fig. S5 [23]), the dispersionless band components with localized states are more responsive to being shifted by variations in the potential strength in comparison to the linear Dirac band components with delocalized states (Supplemental Fig. S10 [23]). Therefore, we can conclude that the competition between the multiperiodic components of the high-order kagome potential results in this dispersion-selective band modulation.

The local-state-induced band evolution is also observed in twisted bilayer graphene, causing slight distortions in the flatbands as the band filling changes [36]. When the Fermi level enters the flatbands, the Hartree interaction introduces a filling-dependent triangular superlattice potential. The real-space states of flatbands at the edges of the moiré Brillouin zone (K orbitals) follow the periodicity of the potential, while the states at the Brillouin zone center (Γ orbitals) form a ring-shaped potential [37,38]. As the band filling of flatbands changes, the triangular localized states become more sensitive to being tuned than the ring-shaped states, leading to slight distortions in the flatbands. Anyway, this kind of band evolution is intricately linked with the band-filling conditions and is not subject to artificial control.

In contrast, we artificially modulate the superlattice potential strength to effectively manipulate the band structures. As shown in Supplemental Fig. S10 [23], when $V_{\text{on-site}}$ increases, all band components move upward with the dispersionless components of the bands ($F1$–$F4$) noticeably faster than the dispersive ones ($D1$ and $D2$). For the IDP, $F1$ and $F3$ shift toward $D1$, resulting in the compression of the Dirac band. On the other hand, for the SDP, $F2$ and $F4$ are elevated away from $D2$, leading to an increase in the Fermi velocity. Taken together, these two effects give rise to a clear spectral weight redistribution of the multiple Dirac bands. This dispersion-selective band engineering is vividly demonstrated by a band-evolution animation calculated by continuous model (Supplemental Video 1 [23]), which aligns well with the tight-bonding results. Compared to previous studies on artificial lattices, our work offers an in-depth understanding of the evolutionary dynamics of band structures under the influence of artificial potentials.

A magnetic field was applied to further investigate the tunability of the artificial kagome lattice. When subjected to a small potential field ($V_{\text{Si}} = -40$ V), a conventional Hofstadter butterfly spectrum is observed (Supplemental Fig. S13 [23]). However, when V_{Si} is large enough to
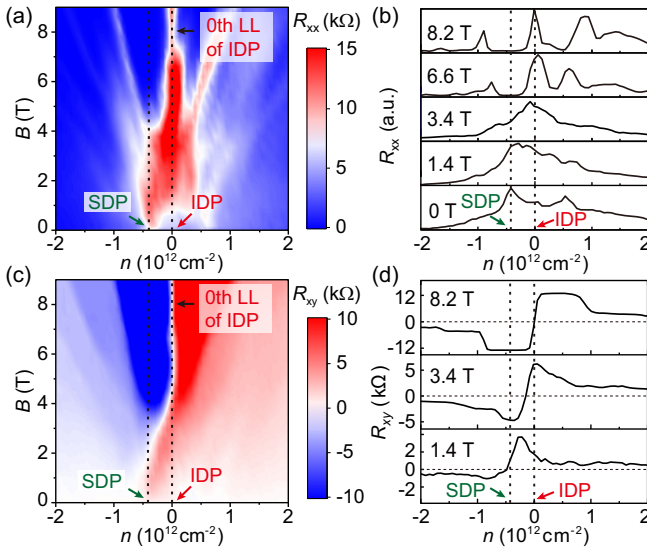
FIG. 4. Spectral weight redistribution of the Dirac bands induced by magnetic field. (a),(b) Longitudinal resistance R_{xx} map as a function of n and B, and corresponding line cuts, at $V_{Si} = -60$ V. (c),(d) Hall resistance R_{xy} map as a function of n and B, and corresponding line cuts. The red and green arrows in (a)–(d) indicate the positions of IDP and SDP, respectively.

suppress the IDP, the magnetic field can substantially weaken the superlattice impact, thereby reactivating the IDP. Figure 4 presents the evolution of longitudinal and Hall resistances with increasing the perpendicular magnetic fields (B) at $V_{Si} = -60$ V. At small magnetic fields, the resistance peak of the IDP remains absent, with the resistive extremum primarily driven by the left SDP. As B increases, the longitudinal resistance maximum gradually shifts from the SDP to the IDP. When B exceeds 4 T, the primary resistance peak is once again governed by the zeroth Landau level (LL) of the IDP, and the SDP becomes invisible. Similarly, from the Hall resistance results, the variation of the CNPs, as indicated by the boundary of the reversed Hall signals, further verifies the evolution of dominant Dirac cones as B increases.

This behavior can be ascribed to the competition between the superlattice potential and the magnetic field. When the Lorentz force caused by the magnetic field exceeds the artificial potential force, it will lead to a form of magnetic breakdown [33,34]. This magnetic breakdown effect disrupts the localized electronic states trapped by the artificial potentials, thereby weakening the superlattice effect. We semiquantitatively analyze the magnetic Hall data at different V_{Si} as shown in Fig. 4(c) and Supplemental Fig. S14 [23]. The transitions of the CNP positions from the SDPs to the IDPs occur within the magnetic field range from ~2 to ~4 T. Such a magnetic field range corresponds to the cyclotron energies $\hbar\omega_c = \sqrt{2}\hbar v_F/\ell_B = v_F\sqrt{2e\hbar B}$ between ~50 and ~70 meV, which is in reasonable agreement with the value of the adopted $V_{on\text{-}site}$ in our band calculation (detailed in Supplemental Note 6 [23]).

In closing, we utilize a specially designed high-order kagome potential to reconstruct band structures through different potential contributions, therefore achieving actively dispersion-selective band engineering. Our findings unveil a new tuning knob for *in situ* and continuous band modulation and represent an in-depth insight into the dynamics of band evolution under the action of artificial potentials. By extending this new concept of band modulation to other unique artificial lattices [39–42] and a richer variety of vdW systems, we may be able to achieve band design at will and potentially realize emergent properties that are not inherent in natural materials.

[1] F. Capasso, Band-gap engineering: From physics and materials to new semiconductor devices, Science **235**, 172 (1987).

[2] H. Kroemer, Nobel lecture: Quasielectric fields and band offsets: Teaching electrons new tricks, Rev. Mod. Phys. **73**, 783 (2001).

[3] M. L. Lee, E. A. Fitzgerald, M. T. Bulsara, M. T. Currie, and A. Lochtefeld, Strained Si, SiGe, and Ge channels for high-mobility metal-oxide-semiconductor field-effect transistors, J. Appl. Phys. **97**, 11101 (2005).

[4] C.-Z. Ning, L. Dou, and P. Yang, Bandgap engineering in semiconductor alloy nanomaterials with widely tunable compositions, Nat. Rev. Mater. 2, 1 (2017).

[5] K. S. Novoselov, A. K. Geim, S. V. Morozov, D. Jiang, M. I. Katsnelson, I. V. Grigorieva, S. V. Dubonos, and A. A. Firsov, Two-dimensional gas of massless Dirac fermions in graphene, Nature (London) 438, 197 (2005).

[6] E. Y. Andrei, D. K. Efetov, P. Jarillo-Herrero, A. H. MacDonald, K. F. Mak, T. Senthil, E. Tutuc, A. Yazdani, and A. F. Young, The marvels of moiré materials, Nat. Rev. Mater. 6, 201 (2021).

[7] Y. Cao, V. Fatemi, A. Demir, S. Fang, S. L. Tomarken, J. Y. Luo, J. D. Sanchez-Yamagishi, K. Watanabe, T. Taniguchi, E. Kaxiras, R. C. Ashoori, and P. Jarillo-Herrero, Correlated insulator behaviour at half-filling in magic-angle graphene superlattices, Nature (London) 556, 80 (2018).

[8] Y. Cao, V. Fatemi, S. Fang, K. Watanabe, T. Taniguchi, E. Kaxiras, and P. Jarillo-Herrero, Unconventional superconductivity in magic-angle graphene superlattices, Nature (London) 556, 43 (2018).

[9] M. Serlin, C. Tschirhart, H. Polshyn, Y. Zhang, J. Zhu, K. Watanabe, T. Taniguchi, L. Balents, and A. Young, Intrinsic quantized anomalous Hall effect in a moiré heterostructure, Science 367, 900 (2020).

[10] C. Tschirhart, M. Serlin, H. Polshyn, A. Shragai, Z. Xia, J. Zhu, Y. Zhang, K. Watanabe, T. Taniguchi, and M. Huber, Imaging orbital ferromagnetism in a moiré Chern insulator, Science 372, 1323 (2021).

[11] J.-X. Lin, Y.-H. Zhang, E. Morissette, Z. Wang, S. Liu, D. Rhodes, K. Watanabe, T. Taniguchi, J. Hone, and J. Li, Spin-orbit–driven ferromagnetism at half moiré filling in magic-angle twisted bilayer graphene, Science 375, 437 (2022).

[12] Z. Zheng, Q. Ma, Z. Bi, S. de la Barrera, M.-H. Liu, N. Mao, Y. Zhang, N. Kiper, K. Watanabe, T. Taniguchi, J. Kong, W. A. Tisdale, R. Ashoori, N. Gedik, L. Fu, S. Y. Xu, and P. Jarillo-Herrero, Unconventional ferroelectricity in moire heterostructures, Nature (London) 588, 71 (2020).

[13] H. Tian, X. Gao, Y. Zhang, S. Che, T. Xu, P. Cheung, K. Watanabe, T. Taniguchi, M. Randeria, F. Zhang, C. N. Lau, and M. W. Bockrath, Evidence for Dirac flat band superconductivity enabled by quantum geometry, Nature (London) 614, 440 (2023).

[14] J. Cai, E. Anderson, C. Wang, X. Zhang, X. Liu, W. Holtzmann, Y. Zhang, F. Fan, T. Taniguchi, K. Watanabe, Y. Ran, T. Cao, L. Fu, D. Xiao, W. Yao, and X. Xu, Signatures of fractional quantum anomalous Hall states in twisted $MoTe_2$, Nature (London) 622, 63 (2023).

[15] Y. Zeng, Z. Xia, K. Kang, J. Zhu, P. Knüppel, C. Vaswani, K. Watanabe, T. Taniguchi, K. F. Mak, and J. Shan, Thermodynamic evidence of fractional Chern insulator in moiré $MoTe_2$, Nature (London) 622, 69 (2023).

[16] H. Park, J. Cai, E. Anderson, Y. Zhang, J. Zhu, X. Liu, C. Wang, W. Holtzmann, C. Hu, Z. Liu, T. Taniguchi, K. Watanabe, J.-h. Chu, T. Cao, L. Fu, W. Yao, C.-Z. Chang, D. Cobden, D. Xiao, and X. Xu, Observation of fractionally quantized anomalous Hall effect, Nature (London) 622, 74 (2023).

[17] S. Wang, D. Scarabelli, L. Du, Y. Y. Kuznetsova, L. N. Pfeiffer, K. W. West, G. C. Gardner, M. J. Manfra, V. Pellegrini, S. J. Wind, and A. Pinczuk, Observation of Dirac bands in artificial graphene in small-period nano-patterned GaAs quantum wells, Nat. Nanotechnol. 13, 29 (2018).

[18] C. Forsythe, X. Zhou, K. Watanabe, T. Taniguchi, A. Pasupathy, P. Moon, M. Koshino, P. Kim, and C. R. Dean, Band structure engineering of 2D materials using patterned dielectric superlattices, Nat. Nanotechnol. 13, 566 (2018).

[19] R. Huber, M.-H. Liu, S.-C. Chen, M. Drienovsky, A. Sandner, K. Watanabe, T. Taniguchi, K. Richter, D. Weiss, and J. Eroms, Gate-tunable two-dimensional super-lattices in graphene, Nano Lett. 20, 8046 (2020).

[20] Y. Li, S. Dietrich, C. Forsythe, T. Taniguchi, K. Watanabe, P. Moon, and C. R. Dean, Anisotropic band flattening in graphene with one-dimensional superlattices, Nat. Nanotechnol. 16, 525 (2021).

[21] D. Barcons Ruiz, H. Herzig Sheinfux, R. Hoffmann, I. Torre, H. Agarwal, R. K. Kumar, L. Vistoli, T. Taniguchi, K. Watanabe, A. Bachtold, and F. H. L. Koppens, Engineering high quality graphene superlattices via ion milled ultra-thin etching masks, Nat. Commun. 13, 6926 (2022).

[22] L. A. Ponomarenko, R. V. Gorbachev, G. L. Yu, D. C. Elias, R. Jalil, A. A. Patel, A. Mishchenko, A. S. Mayorov, C. R. Woods, J. R. Wallbank, M. Mucha-Kruczynski, B. A. Piot, M. Potemski, I. V. Grigorieva, K. S. Novoselov, F. Guinea, V. I. Fal'ko, and A. K. Geim, Cloning of Dirac fermions in graphene superlattices, Nature (London) 497, 594 (2013).

[23] See Supplemental Material at http://link.aps.org/supplemental/10.1103/PhysRevLett.133.066302 for experimental and theoretical details, as well as additional figures and discussions, which includes Refs. [18,19,24–34].

[24] L. Wang, I. Meric, P. Huang, Q. Gao, Y. Gao, H. Tran, T. Taniguchi, K. Watanabe, L. Campos, and D. J. S. Muller, One-dimensional electrical contact to a two-dimensional material, Science 342, 614 (2013).

[25] F. Guinea and T. Low, Band structure and gaps of triangular graphene superlattices, Phil. Trans. R. Soc. A 368, 5391 (2010).

[26] C. Geuzaine and J.-F. Remacle, Gmsh: A 3-D finite element mesh generator with built-in pre- and post-processing facilities, Int. J. Numer. Methods Eng. 79, 1309 (2009).

[27] A. Logg, K.-A. Mardal, and G. Wells, Automated Solution of Differential Equations by the Finite Element Method (Springer, New York, 2012).

[28] M.-H. Liu, Theory of carrier density in multigated doped graphene sheets with quantum correction, Phys. Rev. B 87, 125427 (2013).

[29] H. Shi, Z. Zhan, Z. Qi, K. Huang, E. V. Veen, J. A. Silva-Guillen, R. Zhang, P. Li, K. Xie, H. Ji, M. I. Katsnelson, S. Yuan, S. Qin, and Z. Zhang, Large-area, periodic, and tunable intrinsic pseudo-magnetic fields in low-angle twisted bilayer graphene, Nat. Commun. 11, 371 (2020).

[30] M.-H. Liu, P. Rickhaus, P. Makk, E. Tovari, R. Maurand, F. Tkatschenko, M. Weiss, C. Schonenberger, and K. Richter, Scalable tight-binding model for graphene, Phys. Rev. Lett. 114, 036601 (2015).

[31] Y. Li, Z. Zhan, X. Kuang, Y. Li, and S. Yuan, TBPLaS: A tight-binding package for large-scale simulation, Comput. Phys. Commun. 285, 108632 (2023).

[32] E. Sierda, X. Huang, D. I. Badrtdinov, B. Kiraly, E. J. Knol, G. C. Groenenboom, M. I. Katsnelson, M. Rösner, D. Wegner, and A. A. Khajetoorians, Quantum simulator to emulate lower-dimensional molecular structure, Science **380,** 1048 (2023).

[33] P. H. Beton, E. S. Alves, P. C. Main, L. Eaves, M. W. Dellow, M. Henini, O. H. Hughes, S. P. Beaumont, and C. D. W. Wilkinson, Magnetoresistance of a two-dimensional electron gas in a strong periodic potential, Phys. Rev. B **42,** 9229 (1990).

[34] P. H. Beton, M. W. Dellow, P. C. Main, E. S. Alves, L. Eaves, S. P. Beaumont, and C. D. W. Wilkinson, Magnetic breakdown of a two-dimensional electron gas in a periodic potential, Phys. Rev. B **43,** 9980 (1991).

[35] G. B. Jo, J. Guzman, C. K. Thomas, P. Hosur, A. Vishwanath, and D. M. Stamper-Kurn, Ultracold atoms in a tunable optical kagome lattice, Phys. Rev. Lett. **108,** 045305 (2012).

[36] X. Lu, P. Stepanov, W. Yang, M. Xie, M. A. Aamir, I. Das, C. Urgell, K. Watanabe, T. Taniguchi, G. Zhang, A. Bachtold, A. H. MacDonald, and D. K. Efetov, Superconductors, orbital magnets and correlated states in magic-angle bilayer graphene, Nature (London) **574,** 653 (2019).

[37] F. Guinea and N. R. Walet, Electrostatic effects, band distortions, and superconductivity in twisted graphene bilayers, Proc. Natl. Acad. Sci. U.S.A. **115,** 13174 (2018).

[38] L. Rademaker and P. Mellado, Charge-transfer insulation in twisted bilayer graphene, Phys. Rev. B **98,** 235158 (2018).

[39] C. Wang, F. Liu, and H. Huang, Effective model for fractional topological corner modes in quasicrystals, Phys. Rev. Lett. **129,** 056403 (2022).

[40] S. Sakai, R. Arita, and T. Ohtsuki, Hyperuniform electron distributions controlled by electron interactions in quasicrystals, Phys. Rev. B **105,** 054202 (2022).

[41] E. van Veen, S. Yuan, M. I. Katsnelson, M. Polini, and A. Tomadin, Quantum transport in Sierpinski carpets, Phys. Rev. B **93,** 115428 (2016).

[42] X. Yang, W. Zhou, Q. Yao, P. Lv, Y. Wang, and S. Yuan, Electronic properties and quantum transport in functionalized graphene Sierpinski-carpet fractals, Phys. Rev. B **105,** 205433 (2022).